

First fringes with an integrated-optics beam combiner at $10\ \mu\text{m}$

A new step towards instrument miniaturization for mid-infrared interferometry

L. Labadie^{1,4,5}, G. Martín², N. C. Anheier³, B. Arezki², H. A. Qiao³, B. Bernacki³, P. Kern²

¹ Instituto de Astrofísica de Canarias, C/ Via Lactea s/n, La Laguna, Tenerife E-38200, Spain
e-mail: labadie@iac.es

² UJF-Grenoble 1/CNRS-INSU, Institut de Planétologie et d'Astrophysique de Grenoble (IPAG) UMR 5274, Grenoble, F-38041, France

³ Pacific Northwest National Laboratory, 902 Battelle Boulevard, P.O. Box 999, Richland, Washington 99352, U.S.A

⁴ Departamento de Astrofísica, Universidad de La Laguna, 38205 La Laguna, Tenerife, Islas Canarias, Spain

⁵ I. Physikalisches Institut, Universität zu Köln, Zùlpicher Str. 77, 50937 Köln, Germany

Received September 15, 1996; accepted March 16, 1997

ABSTRACT

Context. Observations at milliarcsecond-resolution scales and high dynamic range hold a central place in the exploration of distant planetary systems to achieve, for instance, the spectroscopic characterization of exo-Earths or the detailed mapping of their protoplanetary discs birthplace. Multi-aperture infrared interferometry, either from the ground or from space, is a very promising technique to tackle these goals. However, significant technical efforts still need to be undertaken to achieve a simplification of these instruments if we want to recombine the light from a large number of telescopes. Integrated-optics concepts appear as an alternative to the current conventional designs, especially if their use can be extended to a higher number of astronomical bands.

Aims. This article reports, for the first time to our knowledge, the experimental demonstration of the feasibility of an integrated-optics approach to mid-infrared beam combination for single-mode stellar interferometry.

Methods. We have fabricated a 2-telescope beam combiner prototype integrated on a substrate of chalcogenide glass, a material transparent from $\sim 1\ \mu\text{m}$ to $\sim 14\ \mu\text{m}$. We have developed laboratory tools to characterize in the mid-infrared the modal properties and the interferometric capabilities of our device.

Results. We obtain interferometric fringes at $10\ \mu\text{m}$ and measure a mean contrast $V=0.981\pm 0.001$ with high repeatability over one week and high stability over a time-period of $\sim 5\ \text{h}$. We show experimentally – as well as on the basis of modeling considerations – that the component has a single-mode behavior at this wavelength, which is essential to achieve high-accuracy interferometry. From previous studies, the propagation losses are estimated to 0.5 dB/cm for this type of component. We also discuss possible issues that may impact the interferometric contrast.

Conclusions. The IO beam combiner performs well at the tested wavelength. We also anticipate the requirement of a better matching between the numerical apertures of the component and the (de)coupling optics to optimize the total throughput. The next step foreseen is the achievement of wide-band interferograms.

Key words. Instrumentation: high angular resolution, interferometers – Methods: laboratory – Techniques: interferometric

1. Introduction

Very recent results have demonstrated the potential of optical/IR interferometers to produce the first infrared astrophysical images of complex morphologies at the milli-arcsecond scale. These images have revealed unprecedented details on the highly distorted photosphere of the fast rotator Altair (Monnier et al. 2007), they have produced the first direct view on the inner regions of a young circumstellar disk (Renard et al. 2010), and have permitted to measure the gas velocity map in the very close surrounding of a supergiant (Millour et al. 2011). Such important breakthroughs would have not been possible without the help of imaging interferometers. Key to this technique is on the astronomers ability to simultaneously and coherently combine the beams from three or more telescopes. This permits the implementation of closure-phase techniques to obtain the interferometric visibilities amplitude and phase and allows reconstruction of a complex astrophysical image. Although other techniques exist to retrieve the necessary phase information, increasing the number of sub-apertures and using Earth-rotation syn-

thesis also drastically improves the UV plane coverage. This provides nearly snapshot reconstructed images, exhibiting high-fidelity and model-independent views of the object. However, the corollary of multi-beam combination is a significant increase in the optical complexity of the interferometer coupled to the need for high instrumental stability (mechanical and thermal) and for a good level of control of the shape of the incoming wavefronts. In the last decade, instrumental research programs have demonstrated the feasibility of *single-mode* integrated optics (IO) components to enable both multi-aperture and high accuracy interferometric instruments using centimeter-scale devices (Malbet et al. (1999) and the following papers series). IO-based solutions have proven their astronomical potential with IOTA/IONIC (Berger et al. 2001; Monnier et al. 2004; Kraus et al. 2005) and VLTI/PIONER, putting them eventually at the heart of the future interferometric instrument GRAVITY at the VLTI. To date, this elegant solution and hence the resulting science has been limited to the near-infrared domain (J, H, K bands), yet there is an unquestionable astrophysical interest to extend this approach to the mid-infrared range, be-

yond $\sim 3\ \mu\text{m}$. This is for instance a key spectral range where to study objects with temperatures of $\sim 100\text{--}600\ \text{K}$ (e.g. the planet forming regions around young solar-type stars, the location of the snow line (Sasselov & Lecar 2000), debris disks morphologies as remnant of the planet formation process). Chemical biomarkers like CO_2 or H_2O could be detected spectroscopically between 5 and $20\ \mu\text{m}$ range to characterize the atmosphere of exoplanets in the habitable zone of solar-type stars (Cockell et al. 2009). In this respect, a space-based mid-infrared and multi-aperture *nuller* able to produce a deep extinction of the stellar light (Angel & Woolf 1997; Mennesson & Mariotti 1997) would benefit as well from the compactness and stability of a IO beam-combiner. These different aspects have motivated a long-term work in the community in order to extend the IO instrumental solution beyond $2\ \mu\text{m}$ (Mennesson et al. 1999; Laurent et al. 2002; Wehmeier et al. 2004; Labadie et al. 2006a, 2007; Hsiao et al. 2009). Because of the relative technological gap historically existing with the more mature near-infrared solutions, the mid-infrared extension has required a concerted R&D research effort between astronomers and photonics experts.

In this study, we demonstrate for the first time the fabrication and the operation of a two-telescope IO single-mode beam combiner for the mid-infrared spectral range around $\lambda=10\ \mu\text{m}$. Chalcogenide glass materials are used for fabrication of this IO device, primarily due to the excellent infrared transparency in the $1\text{--}14\ \mu\text{m}$ range and the photo-induced modification properties, i.e. the permanent or reversible increase of a glass refractive index induced by radiation (light, laser irradiation, etc...). The present work focuses primarily on the achievable interferometric contrasts and on the single-mode characterization of this new component.

2. Component design and manufacturing

2.1. Dimensioning and modal behavior

The opto-geometrical parameters of the Y-junction¹ are chosen to constrain the *single-mode* behavior in the $10\ \mu\text{m}$ spectral range in order to benefit from the necessary spatial filtering of the combined wavefronts. Since a vast bibliography is existing on the advantage of spatial filtering by single-mode waveguides for stellar interferometry and the corresponding theory

¹ The Y-junction is a photonics device which can be used either as a beam-splitting device (1 input, 2 outputs) or as a beam-combiner device (2 inputs, 1 input).

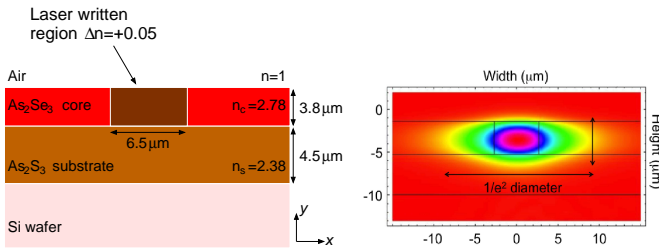


Fig. 1. *Left:* Cross-section view of the Y-junction geometry. The high-index strip waveguide is bounded by As_2Se_3 , As_2S_3 and air. Examples of refractive indices at 6 , 8 , 10 and $12\ \mu\text{m}$ used in this study are: $n=2.788$, 2.783 , 2.777 , 2.774 for As_2Se_3 ; $n=2.403$, 2.394 , 2.381 , 2.364 for As_2S_3 . *Right:* theoretical spatial distribution of the electric field for the $\text{TE}_{0,0}$ fundamental mode superimposed to the waveguide geometry. The vertical scale ranges from high (violet) to low (yellow) intensity.

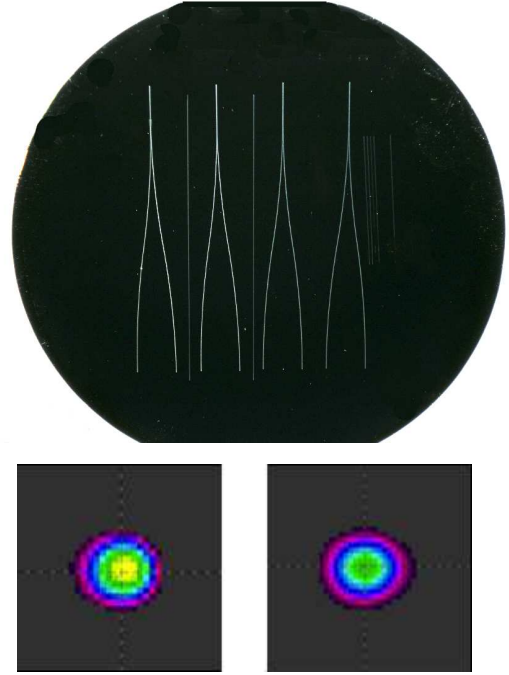


Fig. 2. *Top:* Photo of the wafer containing the Y-junctions and the channel waveguides (see text for details). *Down:* Qualitative snapshot views of the Y-junction outputs imaged at $8.5\ \mu\text{m}$ to validate the beam-splitter configuration. The field mode is unresolved by the optical system.

(see Coude Du Foresto et al. (1997); Mennesson et al. (2002) and citing papers), we do not treat this aspect here. In Fig. 1–left we illustrate the geometry adopted in this study, which refers to an asymmetric strip embedded waveguide configuration. The electric field confinement in the y -direction is ensured by the high-index core layer of As_2Se_3 surrounded by a low-index substrate layer of As_2S_3 and air ($n=1$). The confinement in the x -direction is ensured by an increase of the refractive index of the core layer over a well-defined region of the planar waveguide. The parameters considered to describe theoretically the modal behavior of the channel waveguide are the thickness $d=3.8\ \mu\text{m}$ and width $w=6.5\ \mu\text{m}$ of the strip, a local increase of the refractive index $\Delta n=+0.05$. The refractive index value as a function of the wavelength for As_2Se_3 and As_2S_3 are taken from the literature (Savage (1965); Palik (1985); Klocek (1991); see examples in the caption of Fig. 1). We compute the theoretical bi-mode/single-mode cutoff wavelength – i.e. the wavelength above which only the fundamental mode is propagated – using the effective index approximation approach, which is a classical numerical method in guided optics (Cheng & Lin 1990).

For comparison, the bi-mode/single-mode cutoff is computed both for the *planar* waveguide geometry and for the *channel* waveguide geometry. The last value should also correspond to the cutoff wavelength for the Y-junction. With the parameters of Fig. 1–left, we obtain for the planar waveguide a cutoff value of $8.6\ \mu\text{m}$ and $7.7\ \mu\text{m}$ for the TE and TM polarization of the fundamental mode, respectively. We obtain for the channel waveguide a cutoff value of $8.7\ \mu\text{m}$ (TE) and $7.6\ \mu\text{m}$ (TM) for the fundamental mode, respectively. Beyond these cutoff wavelengths, the guiding structure is single-mode for each respective polarization, and in particular at $\lambda=10.6\ \mu\text{m}$ which is our operating interferometric wavelength in this work.

The fundamental mode $1/e^2$ diameter is $\sim 18\ \mu\text{m}$ and $\sim 9\ \mu\text{m}$

in the horizontal and vertical directions, respectively (see Fig. 1–right). This implies large divergence half-angles ($\sim 40^\circ$) requiring fast coupling optics with numerical apertures of the order of $f/\# \sim 0.7$.

2.2. Fabrication of the Y-junction

The manufacturing of the Y-junction device has benefited from the PNNL² expertise on the design and fabrication of chalcogenide single-mode, low-loss waveguides for the thermal infrared, which spans nominally from $8\text{--}14\ \mu\text{m}$. In two previous studies, Labadie et al. (2006b) and Vigreux-Bercovici et al. (2007) gave evidence of the ability of Arsenic–Sulfide–Selenium (As–S–Se) structures to produce an efficient confinement of infrared radiation at $\lambda=10.6\ \mu\text{m}$. Hô et al. (2006) have demonstrated the fabrication of single-mode *channel* waveguides using multi-layer deposition of arsenic-based thin films followed by laser writing (Efimov et al. 2001) to provide the lateral confinement of the field. The new step was then to fabricate and validate more complex guiding structures useful to mid-infrared stellar interferometry.

A chalcogenide thin film structure was produced through thermal deposition of a $3.8\ \mu\text{m}$ core layer of As_2Se_3 on a $4.5\ \mu\text{m}$ substrate layer of As_2S_3 according to deposition parameters described in Hô et al. (2006). The As_2Se_3 film is the high-index guiding structure with $n_{\text{core}}=2.78$ at $10.6\ \mu\text{m}$ while As_2S_3 forms the substrate with $n_{\text{sub}}=2.38$ at $10.6\ \mu\text{m}$. The lateral confinement was obtained using laser writing at $\lambda=633\ \text{nm}$ and with writing power of $1\ \text{mW}$, that locally photomodified the As_2Se_3 core layer, resulting in increased refractive index. Previous results suggests that the achieved photo-induced index difference is $\Delta n \approx 0.04\text{--}0.05$ under these processing conditions. In order to fabricate waveguides, the As_2Se_3 thin film substrate is translated about the focal plane of the focused writing laser beam using a computer-controlled translation stage moving at a speed of $4\ \text{mm/min}$. The waveguide width is slightly larger than the laser spot size of $\sim 6\ \mu\text{m}$.

The length of the manufactured Y-junctions is $\sim 50\ \text{mm}$ long with a separation of $7\ \text{mm}$ between the two arms. The top image of Fig. 2 shows the set of manufactured Y-junctions on the silicon wafer. This wafer also contains a set of straight waveguides written between the junctions and which are used for testing and alignment purposes. The Y-junction device was first tested for its beam-splitting function by launching light into the single input. The bottom view of Fig. 2 shows the qualitative assessment of the beam-splitting capabilities of the device at $8.5\ \mu\text{m}$. The two Y-junction outputs were captured using an infrared microbolometer camera.

3. Experimental setup and procedure

Two different setups have been used in this work. One is dedicated to the interferometric characterization of the devices at $\lambda=10.6\ \mu\text{m}$, the second one focuses on the modal characterization of the components by Fourier-Transform spectroscopy in the $2\text{--}14\ \mu\text{m}$ range. The general view of the setup is presented in Fig. 3 and we briefly describe it hereafter.

The interferometric unit : S_2 and S_3 are, respectively, the infrared CO_2 at $\lambda=10.6\ \mu\text{m}$ laser and the He-Ne alignment sources. The quarter-wave plate WP transforms the CO_2 flux polarization from a linear to a circular one. The beam-expander BE produces

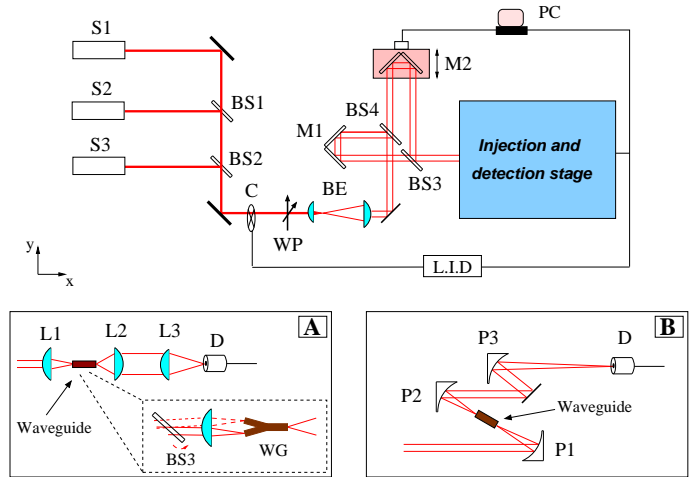


Fig. 3. Schematic view of the characterization testbench. *Top:* S_1 =black body source; S_2 , S_3 =laser sources; BS =beam splitters; C =chopper; WP =quarter-wave plate; BE =beam expander. *Inset–A:* layout for the interferometric characterization; L =lenses; WG =waveguide; D =detector. *Inset–B:* layout for the spectroscopic characterization; P =off-axis parabolas.

a collimated beam of almost 1-inch diameter, which then enters the interferometer. The infrared beam is divided by a system of beam splitters, BS_3 and BS_4 . The mirrors corner cube M_2 is mounted on a motorized translation stage and acts as the delay line to modulate the OPD. It can also be coupled to a piezoelectric motor for fine adjustment. In the monochromatic interferometric configuration, two options are available for waveguide coupling as depicted in the inset A of Fig. 3. One option is to recombine the two beams using BS_3 before injecting into the waveguide. The second option is to slightly tilt BS_3 in order to deviate the beam coming from M_2 , which produces two distinct injection spots. These are used to feed the integrated optics junction, which plays the role of the beam combiner. In this configuration, we simply use refracting optics made in Zinc Selenide (ZnSe). In order to be as much as compliant with the stringent numerical aperture of the current Y-junction inputs, we use an injection lens L_1 with $f/1.1$ clear numerical aperture. The Y-junction output flux is collected by the L_2+L_3 lenses system and focused on the MCT³ detector D . The bench design makes it theoretically symmetric, assuming (M_1 , M_2) and (BS_3 , BS_4) are “equal”, with 3 reflections and 1 transmission per beam.

The spectroscopic unit : it is conceived for broadband spectral characterization of *channel* waveguides as depicted in inset B of Fig. 3. Its configuration is very similar to the interferometric unit, but separately fed by the black-body source S_1 to cover the range from $2\ \mu\text{m}$ to $14\ \mu\text{m}$. Hence, the light injection and collection optical system is based on off-axis parabolas (P_1 , P_2 , P_3) because of their achromatic nature. The broadband fringe pattern is produced by scanning the M_2 corner cube system.

The detection unit : The detection chain is composed of the MCT detector itself, the beam chopper C to modulate the signal and a classical lock-in amplifier. The detected signal is digitally converted by the ADC card and recorded at a typical frequency of $10\ \text{Hz}$ or faster. The experiment takes place in open-air environment, with no active control of the OPD or the beam jitter. Our measurements can potentially be sensitive to air turbulence or mechanical micro-vibrations in the room.

² PNNL: Pacific Northwest National Laboratory

³ MCT or Mercury-cadmium-telluride.

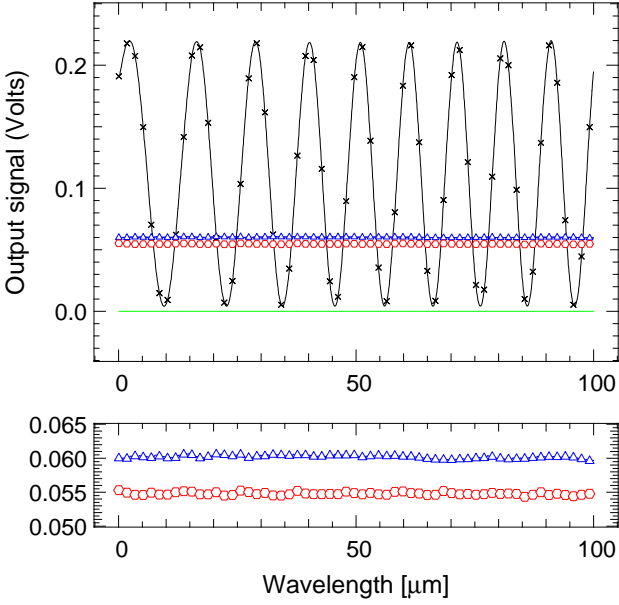


Fig. 4. *Top:* Interferometric scan obtain with the Y-junction at $10.6\mu\text{m}$ (black line+crosses); Photometry 1 (red curve with circles); Photometry 2 (blue curve with triangles); Bias signal (green solid line). *Bottom:* Zoom on the photometric channels 1 and 2 in each arm of the Y-junction over the same OPD range as for the interferometric signal.

In the future, we plan the development of a test-bench which allows us a direct coupling of the individual beams in the component without passing by the external beam-splitters BS_3 and BS_4 , or to explore the viability of a fiber-link IO component (e.g. Berger et al. (1999); Haguenaer et al. (2000)) exploiting the development of single-mode chalcogenide fibers (Ksendzov et al. 2007; Houizot et al. 2007). This aspect is particularly important in view of multi-beam combination.

4. Results and discussion

The Y-junction is the key element of an integrated-based mid-infrared interferometer. The important physical quantities to be characterized for our prototype at this stage are the achievable interferometric contrast and the single-mode operation range. Other interesting parameters to be studied in the future will be the total throughput, the aging effect of the component and the impact of operation at cryogenic temperatures.

4.1. Temporally encoded fringes and monochromatic interferometric contrast

The Y-junction beam combiner has been characterized in the mid-infrared using the P_{22} line ($10.611\mu\text{m}$) of a CO_2 laser. The setup described above permits us to inject flux in both channels, while the OPD is temporally modulated using the scanning delay line. The plots of Fig. 4 shows the monochromatic sinusoidal fringe pattern obtained by scanning 8 periods. The photometric signal from each of the two channels is plotted around 0.05V as a function of the OPD. The bias current of the detector is plotted as well, although its very low level ($\sim 10\mu\text{V}$) has a negligible effect on the calibration. The fringe pattern displays a small chirp effect – i.e. a broadening of the period – from 0 to $100\mu\text{m}$, resulting from known small non-linearities of the translation stage. However, this has no

great impact on the reliability of the measurement. The bottom plot of Fig. 4 shows a zoom on the photometry to illustrate the small photometric unbalance between the two input channels. In the following, the photometry unbalance is defined by $\rho = 1 - (I_1/I_2)$ with I_1 being the weakest flux, so $\rho = 0$ for a perfectly balanced system. In the case of Fig. 4, the plotted curves present an unbalance of $\rho \approx 9\%$, which is then expected to have a negligible effect on the improvement of the interferometric contrast. Note that this last remark does not hold anymore if deep interferometric nulling is targeted, as demonstrated in Labadie et al. (2007). However, the work presented here does not focus on optimized nulling measurement, but rather on the feasibility of an IO approach for mid-infrared interferometry.

In our specific case of a point-like source, the canonical expression for the monochromatic intensity interferogram is $I(x) = I_1(x) + I_2(x) + 2\sqrt{I_1(x)I_2(x)}\cos(\phi(x))$ where I , I_1 , I_2 are the interferometric, photometry 1, photometry 2 signals respectively. The quantity ϕ is the phase delay and x the OPD. The photometrically calibrated interferogram $I_{\text{cor}}(x)$ is simply given by $I_{\text{cor}}(x) = (I(x) - I_1(x) - I_2(x)) / (2\sqrt{I_1(x)I_2(x)})$. $I'(x) = 1 + I_{\text{cor}}(x)$ is the normalized interferogram that would correspond to the observed signal if there were no photometric unbalance. The interferometric contrast can then be estimated in different ways, which essentially depends on the monochromatic or polychromatic conditions. We experimentally measure the raw and calibrated contrasts through $V = (I_{\text{max}} - I_{\text{min}}) / (I_{\text{max}} + I_{\text{min}})$ and $V_{\text{cor}} = (I'_{\text{max}} - I'_{\text{min}}) / (I'_{\text{max}} + I'_{\text{min}})$. The *min* and *max* indices correspond to the maximum and minimum values for the sine signal.

The plots of Fig. 5 illustrate the results of the interferometric calibration at two different dates, October 6 and October 14, 2010, respectively. The error bar associated to each visibility point is estimated through the propagation of experimental errors associated to the I_{max} and I_{min} quantities. In the top panel

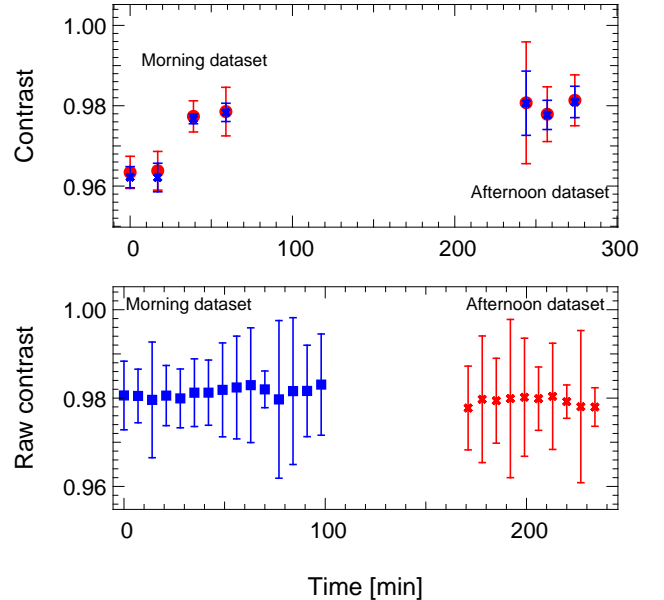


Fig. 5. *Top:* Raw (blue crosses, V) and calibrated (red filled circles, V_{cor}) visibilities measured from the dataset of October 14, 2010. *Bottom:* Evolution as a function of time of the raw contrast obtained with the Y-junction on the dataset of October 6, 2010. The visibility points dispersion around the mean value is ± 0.001 .

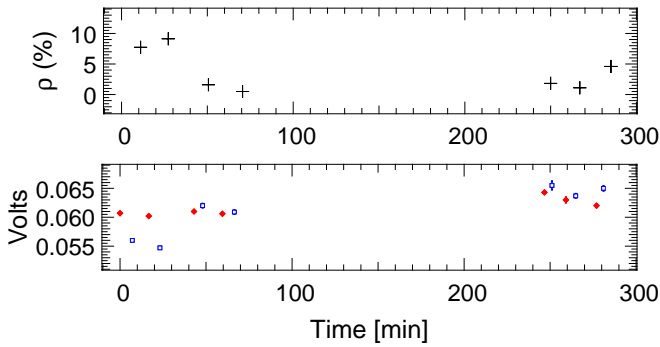


Fig. 6. *Top:* Evolution as a function of time of the photometric unbalance between the two arms of the Y-junction. *Bottom:* Evolution as a function of time of the mean and error of the photometry-1 (blue open squares) and photometry-2 (filled red diamonds) signals. In most cases, the error bar is equal or smaller than the symbol itself.

of Fig. 5, we have compared the results on the raw visibilities V (blue crosses) to the photometry-calibrated visibilities V_{cor} (red filled circles) over several hours. Each interferometric scan was interleaved with successive acquisitions of the photometry channels I_1 and I_2 under the same conditions of OPD scan. The individual interferometric visibilities span from 0.96 to 0.98. They appear slightly more fluctuating in the first 50 min, then stabilizing around 0.98. We can notice that the photometric calibration has little or no impact on the measured interferometric contrast, which is due to the small photometric unbalance of less than 10% (see Fig. 6) or a theoretical degradation of 0.001 of the interferometric contrast. The bottom panel of Fig. 5 shows a better sampling of the temporal variations of the raw visibilities V on time scales of ~ 10 min. The interferometric contrast appears very stable to 0.1% over 5 h, with a time-averaged estimate of $V=0.981\pm 0.001$. Here, the errors propagation method applied for each data does not appear to reflect the effective stability of the experimental visibilities, which dispersion is smaller than the individual error bars.

Our experimental measurements clearly show that the Y-junction can successfully recombine interferometrically infrared beams and deliver high and stable contrasts. It is also interesting for future studies to anticipate on other issues potentially affecting the interferometric performance.

– A first consideration is on the possible polarization mismatches that can diminish the interferometric visibility. The polarization states in the two channels are not monitored in this experiment. From Traub (1988), we know that a phase shift of 22.5° between the s - p differences of the two beams would be sufficient to introduce a visibility drop of $V=0.02$ (s and p being the perpendicular and parallel components in the xy plane of incidence). Although this could be a considerable loss for future high contrast interferometric measurements, it remains quite acceptable for traditional V^2 interferometry. Such a small phase shift could be either produced by the bench optics (despite the apparent symmetry of the interferometer) or by differential effects in the Y-junction arms. As an aside remark, we remind that the high dynamic range shown in Labadie et al. (2007) was obtained using a single-mode *and* single-polarization waveguide. Although not trivial, different practical solutions could be implemented on the bench to explore the polarization

state of the combined beams before and after their coupling into the Y-junction.

– A second and more general consideration can be made on the single-mode behavior of the Y-junction. If we assume that the component is not “perfectly” single-mode – i.e. that the first higher-order mode is not completely filtered out because we are too close to the cutoff for instance – then we will experience residual phase errors (small misalignments, optical surfaces defects) that would not be compensated with the photometric calibration (in other words, the waveguide does not perform perfectly well the flattening of the wavefront). Because the single-mode behavior at a given λ is only depending on the component properties, its design must be carefully implemented to delimit the suitable single-mode range. Eventually, a detailed analysis of the spatial distribution and propagation of the different modes in the structure as a function of the wavelength would certainly be helpful, although not critical at this stage. The question of the modal behavior is addressed in the following section.

4.2. Spectroscopic characterization of the modal behavior

As explained in Sect. 1, the single-mode feature of the Y-junction is essential for an efficient spatial filtering of the incoming wavefront. In order to take advantage of the wavefront filtering capabilities of the component, it is therefore necessary to assess the spectral region where solely one mode is guided through the waveguide. By definition, the component presents several cutoff wavelengths, which defines different modal regimes (e.g. tri-mode, bi-mode, single-mode). These different regions can be evidenced through the *transmitted power method* (Lang et al. 1994), a technique routinely used for the characterization of single-mode fibers, and implemented as well in the field of astronomical instrumentation (Laurent et al. 2002). The principle of this method is based on the idea that the energy coupled into the waveguide at a given wavelength is distributed among the different propagation modes supported by the waveguide. As the wavelength varies from shorter to longer values, the number of supported modes decreases by one at each cutoff wavelength, and this can be traced in a transmission spectrum through the identification of an abrupt dip in the guided flux intensity (Grille et al. 2009).

This technique has been used here to characterize the modal behavior of the channel waveguides visible in Fig. 2 next to the Y-junction, which were manufactured following the same procedure. We verified the single-mode behavior of the component at $10\mu\text{m}$ by doing Fourier Transform spectroscopy between 2 and $14\mu\text{m}$ with the setup described in Sect. 3. The bottom plot of Fig. 7 shows a zoom on the central white light fringe, which is acquired over a total OPD length of 2 mm resulting in a spectral resolution $\Delta\nu=5\text{ cm}^{-1}$. We have produced one reference spectrum of the black body source to be compared with the waveguide spectra, which both are presented in the top panels of Fig. 7.

The blue curve in the top panel is the raw emission spectrum of the black-body source acquired in the sensitivity range of the MCT detector. It includes the transmission by the lab atmosphere and the testbench components. Typical features can be observed such as the CO_2 absorption line around $4.2\mu\text{m}$ or the water vapor absorption lines after $2.5\mu\text{m}$ and between $5\mu\text{m}$ and $7\mu\text{m}$. In the top-mid panel, the green and red curves are, under same experimental conditions, two different measurements of the previous spectrum after coupling light into the chalcogenide chan-

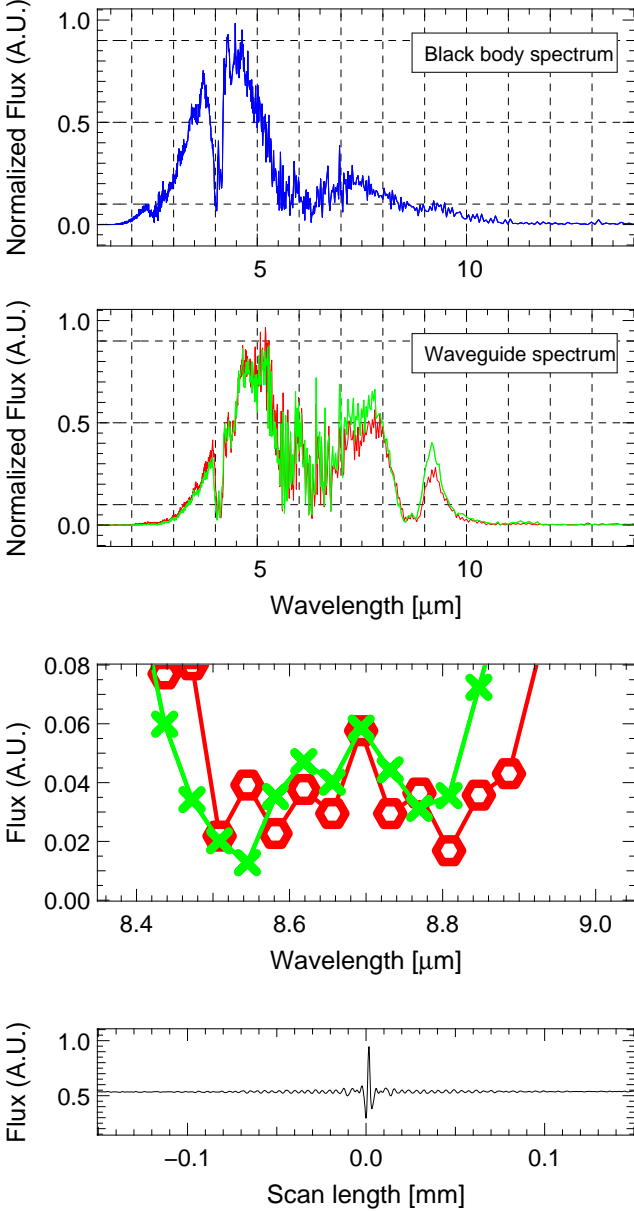


Fig. 7. *Top:* Raw spectrum of the black-body source in the 2–14 μm range. *Central-top:* Two measurements (red and green curves) of the black-body source spectrum after coupling into a chalcogenide channel waveguide with opto-geometrical parameters similar to the Y-junction ones. *Central-bottom:* Zoom on the single-mode cutoff wavelength region. *Bottom:* Zoom on the typical white light interferogram obtained with the FTS.

nel waveguide. The black body and waveguide spectra have been normalized to their peak intensity: indeed, because of the detection parameters (i.e. gain of the lock-in amplifier) that changed between the two measurements, the two curves cannot be compared directly. Here the goal is limited to the identification of *relative* variations in the spectrum resulting from the waveguide characteristics.

The “waveguide” spectra include transmission effects related to the coupling input and output coupling efficiency, to the transparency of the As_2Se_3 glass (i.e. propagation losses), and to the

modal behavior of the waveguide which is precisely the sought effect. On this last point, as this effect results from the loss of successive propagation modes from shorter to longer wavelengths, the amplitude of the transmission dip will be stronger as we go towards the lower order cutoff wavelengths. Hence, we have chosen to focus here only on the search for the deepest bi-mode/single-mode transition since higher order shallower jumps at shorter wavelengths would be more difficult to identify among the several features present in the spectrum. Therefore, the *transmitted power method* comes as a supporting technique to experimentally trace, in a restricted spectral range, the modal characteristics inferred theoretically, rather than a method for blind-searches of cutoff frequencies.

The waveguide plots of Fig. 7 reveal a clear intensity drop from $\sim 8.0 \mu\text{m}$ down to $\sim 8.5 \mu\text{m}$ in both measurements of the waveguide spectrum. A small double-dip feature is observable at $\sim 8.5\text{--}8.6 \mu\text{m}$ and $\sim 8.8 \mu\text{m}$ before the curve rises up. A large intrinsic absorption feature is very unlikely considering the homogeneous transparency of these chalcogenide glasses in this wavelength range (Savage 1965; Moynihan 1975). Then, a possible interpretation is that we observe the bi-mode/single-mode transition of the waveguide with a measured cutoff around $8.5 \mu\text{m}$. The rise-up of the curve afterwards $8.8 \mu\text{m}$ corresponds to the well-known effect of energy transfer from first order to the fundamental mode following the cutoff. The double-dip feature observed at $8.6 \mu\text{m}$ and $8.8 \mu\text{m}$ in the waveguide spectrum may actually correspond to the close signatures of the planar and the channel waveguide, theoretically expected at $8.6 \mu\text{m}$ and $8.7 \mu\text{m}$. Indeed, because the injection spot of the FTS setup is currently considerably larger than the channel waveguide cross-section ($\sim 30 \mu\text{m}$ vs. $\sim 5 \mu\text{m}$), a non-negligible fraction of the input energy is likely coupled into the surrounding planar waveguide, rather than solely in the channel waveguide, and collected back onto the detector. In this hypothesis, we find for the TE polarization a good agreement between the experimental and the theoretical values derived in Sect. 2.1, which are intrinsically very close. The $0.1 \mu\text{m}$ shift in the cutoff wavelength between theory and experience is within the range of uncertainty introduced by the manufacturing process on the index difference Δn and on the physical size of the waveguide, which ultimately define the modal behavior. Being able later to reduce the spot size, keeping at the same time a good signal-to-noise ratio, would certainly help to minimize this effect. For the TM polarization, the cutoff wavelength is expected by design at $7.7 \mu\text{m}$, i.e. in a spectral region where we do not benefit from a good SNR due to the water absorption band. This suggests that the TM cutoff signature may be hidden in the quite noisy region of the spectrum. Eventually, in the solid hypothesis of an observed cutoff wavelength and in spite of the small uncertainty raised above, this result confirms experimentally the single-mode behavior of the manufactured structure around $\lambda=10 \mu\text{m}$.

5. Conclusion

– We conducted a first laboratory study at $10 \mu\text{m}$ of the interferometric capabilities of a single-mode integrated-optics beam combiner in the context of instrumentation activities for multi-aperture IR interferometry. The Y-junction, manufactured by laser-writing, is composed of chalcogenide glasses, which transparency is useful for integrated-optics beam combination in the L ($3.2 \mu\text{m}$), L' ($3.8 \mu\text{m}$), M ($4.5 \mu\text{m}$) and N ($10 \mu\text{m}$) bands.

– We have demonstrated a high fringe contrast of 0.981 ± 0.001 at $\lambda=10.6 \mu\text{m}$, with high repeatability. The fringe contrast shows to

remain very stable over a significant time period of 5 h, and even between two consecutive weeks. The component is also quite stable with regards to photometry variations (Fig. 6-bottom) possibly resulting from time dependent laser drifts, mechanical instabilities of the motorized delay light impacting light coupling into the waveguides, or thermal instabilities of the laboratory environment. We also verified and experimentally confirmed the single-mode range of the device beyond 8.5 μm .

– In this study, we have also experienced the importance of a proper numerical aperture optimization between the coupling optics and the waveguide structure. Large throughput losses occur from both the numerical aperture mismatch and the Fresnel losses at each facet. The magnitude of these losses was not evaluated in this study. We are confident this can be solved by a well-coordinated design of the component and of the interface optics at the telescope. However, we already know from previous studies (Hô et al. 2006) that the intrinsic propagation losses of this type of device are as low as ~ 0.5 dB/cm. This is promising for the immediate future, where wide-band interferometric fringes constitute the next objective.

Although additional research in this area is required, this study can be seen as a first step towards the design, fabrication, and optimization of future instruments that exploit the benefits of astro-photonics (Bland-Hawthorn & Kern 2009) at mid-infrared wavelengths. This work also shows that we are not so far from a new important milestone that could be the on-sky validation of this elegant approach on an operating interferometer. On the longer term, the development of balloon-borne prototype interferometer at mid-infrared wavelengths comparable to what is already being achieved in the far-IR (Shibai et al. 2010) could probably benefit from such advances.

Acknowledgements. LL is funded by the Spanish MICINN under the Consolider-Ingenio 2010 Program grant CSD2006-00070:First Science with the GTC (www.iac.es/consolider-ingenio-gtc). This work was also supported by the U.S. Department of Energy, Office of Nonproliferation Research and Development (NA-22). Pacific Northwest National Laboratory is operated for the U.S. Department of Energy by Battelle Memorial Institute under Contract No. DE-AC05-76RLO1830.

References

- Angel, J. R. P. & Woolf, N. J. 1997, *ApJ*, 475, 373
 Berger, J. P., Haguenaer, P., Kern, P., et al. 2001, *A&A*, 376, L31
 Berger, J. P., Rousselet-Perraut, K., Kern, P., et al. 1999, *A&AS*, 139, 173
 Bland-Hawthorn, J. & Kern, P. 2009, *Optics Express*, 17, 1880
 Cheng, Y. & Lin, W. 1990, *Microwave and Optical Technology Letters*, 3, 419
 Cockell, C. S., Léger, A., Fridlund, M., Herbst, T., & Kaltenecker, L. 2009, *Astrobiology*, 9, 1
 Coude Du Foresto, V., Ridgway, S., & Mariotti, J.-M. 1997, *A&AS*, 121, 379
 Grille, R., Martin, G., Labadie, L., et al. 2009, *Optics Express*, 17, 12516
 Haguenaer, P., Berger, J., Rousselet-Perraut, K., et al. 2000, *Appl. Opt.*, 39, 2130
 Hô, N., Phillips, M. C., Qiao, H., et al. 2006, *Optics Letters*, 31, 1860
 Houizot, P., Boussard-Plédel, C., Faber, A. J., et al. 2007, *Optics Express*, 15, 12529
 Hsiao, H., Winick, K. A., Monnier, J. D., & Berger, J. 2009, *ArXiv e-prints*
 Klocek, P. 1991, *Handbook of infrared optical materials (Optical Engineering, New York: Dekker)*, 428–431
 Kraus, S., Schloerb, F. P., Traub, W. A., et al. 2005, *AJ*, 130, 246
 Ksendzov, A., Lay, O., Martin, S., et al. 2007, *Appl. Opt.*, 46, 7957
 Labadie, L., Labeye, P., Kern, P., et al. 2006a, *A&A*, 450, 1265
 Labadie, L., Le Coarer, E., Maurand, R., et al. 2007, *A&A*, 471, 355
 Labadie, L., Vigreux-Bercovici, C., Pradel, A., et al. 2006b, *Optics Express*, 14, 8459
 Lang, T., Thevenaz, L., Ren, Z. B., & Robert, P. 1994, *Measurement Science and Technology*, 5, 1124
 Laurent, E., Rousselet-Perraut, K., Benech, P., et al. 2002, *A&A*, 390, 1171
 Malbet, F., Kern, P., Schanen-Duport, I., et al. 1999, *A&AS*, 138, 135

- Mennesson, B. & Mariotti, J. M. 1997, *Icarus*, 128, 202
 Mennesson, B., Mariotti, J. M., Coudé du Foresto, V., et al. 1999, *A&A*, 346, 181
 Mennesson, B., Ollivier, M., & Ruilier, C. 2002, *Optical Society of America Journal A*, 19, 596
 Millour, F., Meilland, A., Chesneau, O., et al. 2011, *A&A*, 526, A107
 Monnier, J. D., Traub, W. A., Schloerb, F. P., et al. 2004, *ApJ*, 602, L57
 Monnier, J. D., Zhao, M., Pedretti, E., et al. 2007, *Science*, 317, 342
 Moynihan, C. 1975, *Journal of Non Crystalline Solids*, 17, 369
 Palik, E. D. 1985, *Handbook of optical constants of solids (Academic Press Handbook Series, New York)*, 623–663
 Renard, S., Malbet, F., Benisty, M., Thiébaud, E., & Berger, J. 2010, *A&A*, 519, A26
 Sasselov, D. D. & Lecar, M. 2000, *ApJ*, 528, 995
 Savage, J. 1965, *Infrared Physics*, 5, 195
 Shibai, H., Fukagawa, M., Kato, E., et al. 2010, in *Astronomical Society of the Pacific Conference Series*, Vol. 430, *Astronomical Society of the Pacific Conference Series*, ed. V. Coudé Du Foresto, D. M. Gelino, & I. Ribas, 541–+
 Traub, W. A. 1988, in *European Southern Observatory Conference and Workshop Proceedings*, Vol. 29, *European Southern Observatory Conference and Workshop Proceedings*, ed. F. Merkle, 1029–1038
 Vigreux-Bercovici, C., Bonhomme, E., Pradel, A., et al. 2007, *Applied Physics Letters*, 90, 011110
 Wehmeier, U. J., Swain, M. R., Drouet D’Aubigny, C. Y., Golish, D. R., & Walker, C. K. 2004, in *New Frontiers in Stellar Interferometry, Proceedings of SPIE Volume 5491*, 1435–1444